Wireless Picosecond Time Synchronization for Distributed Antenna Arrays

Jason M. Merlo[®], *Graduate Student Member, IEEE*, Serge R. Mghabghab[®], *Member, IEEE*, and Jeffrey A. Nanzer[®], *Senior Member, IEEE*

Abstract—Distributed antenna arrays have been proposed for many applications ranging from space-based observatories to automated vehicles. Achieving good performance in distributed antenna systems requires stringent synchronization at the wavelength and information levels to ensure that the transmitted signals arrive coherently at the target, or scattered and received signals can be appropriately processed via distributed algorithms. In this article, we address the challenge of high-precision time synchronization to align the operations of elements in a distributed antenna array and overcome time-varying bias between platforms primarily due to oscillator drift. We use a spectrally sparse two-tone waveform, which obtains approximately optimal time estimation accuracy, in a two-way time transfer process. We also describe a technique for determining the true time delay using the ambiguous two-tone matched filter output, and we compare the time synchronization precision of the two-tone waveform with the more common linear frequency modulation (LFM) waveform. We experimentally demonstrate wireless time synchronization using a single-pulse 40-MHz two-tone waveform over a 90-cm 5.8-GHz wireless link in a laboratory setting, obtaining a timing precision of 2.26 ps.

Index Terms—Clock synchronization, distributed arrays, distributed beamforming, radar, remote sensing, two-way time transfer, wireless sensor networks, wireless synchronization.

I. INTRODUCTION

ISTRIBUTED antenna arrays are rapidly evolving as an essential enabling technology for a variety of novel applications ranging from next-generation radio astronomy observatories, small-sat multiple-input—multiple-output (MIMO) communication relays[1, TX05.2.6, TX08.2.3], and planetary remote sensing[2, TA 5.6.7], to collaborative automated vehicle (AV) environmental imaging[3]. Distributed antenna arrays (see Fig. 1) have a number of benefits over

Manuscript received 16 June 2022; revised 13 September 2022; accepted 26 October 2022. Date of publication 20 December 2022; date of current version 4 April 2023. This work was supported in part by the U.S. Department of Energy by the Lawrence Livermore National Laboratory under Contract DE-AC52-07NA27344, in part by the LLNL-LDRD Program under Project 22-ER-035, in part by the Office of Naval Research under Grant N00014-20-1-2389, and in part by the National Science Foundation under Grant 1751655. (Corresponding author: Jeffrey A. Nanzer.)

Jason M. Merlo and Jeffrey A. Nanzer are with the Department of Electrical and Computer Engineering, Michigan State University, East Lansing, MI 48824 USA (e-mail: merlojas@msu.edu; nanzer@msu.edu).

Serge R. Mghabghab was with the Department of Electrical and Computer Engineering, Michigan State University, East Lansing, MI 48824 USA. He is now with MathWorks, Natick, MA 01760 USA (e-mail: mghabgha@msu.edu). Color versions of one or more figures in this article are available at https://doi.org/10.1109/TMTT.2022.3227878.

Digital Object Identifier 10.1109/TMTT.2022.3227878

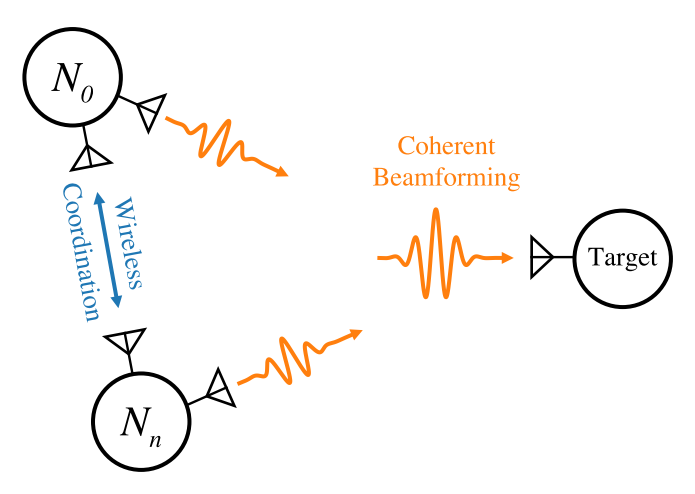


Fig. 1. Distributed antenna array schematic. Distributed antenna nodes coordinate wirelessly to align time, frequency, and phase to achieve coherent information summation at the target location.

traditional platform-centric approaches. In conventional singleplatform systems, obtaining greater performance requires increasing the aperture size, the power limit or efficiency of the amplifiers, or similar means. However, these approaches are limited by device technologies and platform size, among others, making it increasingly challenging to improve wireless performance. In a distributed array architecture, many smaller nodes can be used to synthesize the required gain, potentially at a much lower cost than a monolithic array. In addition, the distributed nature of the system ensures that the array is resilient to node failures or interference, is, furthermore, reconfigurable and adaptable, and can, thus, meet dynamic requirements. In these new distributed aperture applications, however, it is critical that the time, phase, and frequency of the nodes in the array are carefully synchronized to ensure coherent summation of the signal carrier frequencies and alignment of the information envelope at a given target location [4]. While there have been many significant advances in the areas of wireless time, frequency, and phase coordination between nodes in distributed arrays, there are still significant advances required in each of these areas to enable the continuous high-accuracy coordination required to provide coherent operation at millimeter-wave frequencies and multigigahertz information bandwidths. In particular, for modulated waveforms with wide bandwidth, accurate time alignment, i.e., clock synchronization, is critical to ensure high coherent gain at the target location [5].

0018-9480 © 2022 IEEE. Personal use is permitted, but republication/redistribution requires IEEE permission. See https://www.ieee.org/publications/rights/index.html for more information.

While optical means have been used for disciplining remote oscillators and clock alignment wirelessly to femtosecond and subfemtosecond levels by exploiting the large available bandwidth, typically in the terahertz [6], [7], [8], the pointing and tracking tolerance for moving targets is very tight, making it significantly more difficult to implement for dynamic links; in addition, the size, weight, and cost of free-space optical systems are often higher than for microwave and millimeterwave systems. Because of these limitations to optical links, it is of interest to develop microwave and millimeter-wave wireless time synchronization techniques. There have been many prior works focusing on microwave and millimeter-wave time synchronization of wireless sensor networks (WSNs) [9], [10], [11]; however, these have focused primarily on achieving synchronization at the protocol level, in some cases with hardware timestamping at the media access control (MAC) layer [11] to reduce timing uncertainties, but were primarily motivated by synchronization of higher level protocols and data logging where coordination at the microsecond level was sufficient. The more stringent requirements of distributed beamforming and high bandwidth communications necessitate improvements of several orders of magnitude over previous WSN techniques. In recent years, this has been approached via increased signal bandwidth. One recent approach implements a wireless White Rabbit-based protocol using a V-band carrier with a 1.6-GHz bandwidth to achieve a precision of <2 ps over a \sim 500-m line of sight (LoS) link [12]. Another approach using 50-MHz linear frequency modulation (LFM) waveforms recently achieved synchronization precision of 11.3 ps with a signal-to-noise ratio (SNR) of 31.2 dB in an outdoor LoS environment [13]. The third approach using an "enhanced timestamping" cross correlation approach on top of the IEEE 802.11n wireless local area network (LAN) (WLAN) standard with a carrier frequency of 2.412 GHz and 20-MHz bandwidth achieved a timing precision of approximately 650 ps [14].

In this article, we demonstrate a new technique for the high-precision estimation of time delay in a two-way time transfer system for distributed array applications. By utilizing a spectrally sparse two-tone waveform, it is shown that the mean-squared bandwidth of the time delay estimation waveform may be maximized, which yields the maximum theoretical accuracy for time delay estimation. Using this waveform, we experimentally demonstrate a wireless time synchronization precision of <2.5 ps using single-pulse time estimation with a waveform bandwidth of 40 MHz in commercial software-defined radios (SDRs). This work is the first to demonstrate the use of a spectrally sparse two-tone waveform in a fully wireless coordination approach. In prior work, we briefly introduced a two-way time synchronization approach using a two-tone waveform [15]; however, that work required the use of a cabled frequency reference. Here, we combine wireless time transfer with wireless frequency locking to provide a fully wireless approach and demonstrate the ability to obtain picosecond-level time synchronization between nodes. We provide a significantly more detailed description of the system implementation, discussing the time-delay estimation processes used, their challenges, and techniques to mitigate the challenges. We also describe the Cramer–Rao lower bound (CRLB) for time delay estimation and how to maximize the accuracy of the time delay waveform to achieve the theoretical maximum accuracy for a given signal bandwidth and SNR. Finally, we present fully cabled and fully wireless time and frequency synchronization experiments and compare their relative performance to the CRLB. We, furthermore, evaluate the long-term beamforming channel bias measurements to demonstrate the long-term system synchronization bounds due to the current hardware limitations.

The rest of this article is organized as follows. In Section II, we introduce the system time model and two-way time synchronization process and then proceed with the derivation of the CRLB for time delay estimation of the conventional LFM and two-tone waveforms, and finally, we discuss our two-step delay estimation process. In Section III, we discuss the details of frequency synchronization in distributed arrays and the approach used in this article. Finally, in Section IV, we discuss the system hardware configuration and the results of the time-transfer precision experiments for two-tone waveforms over a range of SNR levels for three cases: fully cabled, wireless time transfer with cabled frequency transfer, and fully wireless time-frequency transfer scenarios. Finally, we provide a comparison of other wireless microwave and millimeter-wave time transfer methods as a benchmark for the proposed technique using spectrally sparse waveforms.

II. DISTRIBUTED ANTENNA ARRAY TWO-WAY TIME SYNCHRONIZATION

Generally, two types of techniques are commonly employed to synchronize distributed clocks: one-way methods and twoway methods. The most common technique for wireless time transfer is one way as it is employed by many of the global navigation satellite system (GNSS) constellations in orbit today for time distribution where the GNSS satellite acts as a "primary" clock source, and all the receiver nodes synchronize their clocks to the primary source after solving for the propagation delay of the signal based on the ephemeris provided by each satellite and the known position of the receiver [16]. The difficulty of this process is that either the receiver and transmitter's positions must both be known or multiple sources with known positions are required to solve for the propagation delay. An alternative approach is two-way time synchronization, which inherently solves for both the time of flight and clock offset, assuming a quasi-static channel during the synchronization epoch; the two-way time transfer technique has been used for satellite time transfer for many decades to synchronize satellites to ground clocks and with other satellites [17], [18], [19]. A more recent protocol that uses two-way time transfer is precision time protocol (PTP), which achieves timing precision on the order of 1 μ s; PTP is also the foundation for the White Rabbit protocol, a popular industrial synchronous Ethernet protocol that acts as a refinement on the PTP estimation by using the carrier phase of Ethernet over fiber to determine residual time delay with high precision, typically on the order of 10 ps [20]. However, the White Rabbit protocol is designed to work over fiber and, thus, cannot be used on its own to coordinate wirelessly.

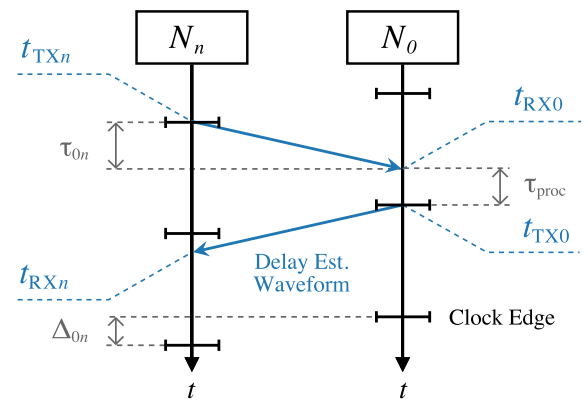


Fig. 2. Two-way time transfer timing diagram. Node N_n initiates time transfer with the primary node, N_0 ; a delay estimation waveform is transmitted from node N_n to N_0 and back with timestamps saved at each transmission and reception. From the four timestamps, a time offset and internode distance can be computed using (3) and (4), respectively, assuming that the channel was quasi-static over the synchronization epoch (i.e., between t_{TX_n} and t_{RX_n}).

A. System Model

In general, a distributed array system can be modeled as a set of N nodes, each of which has a local clock, which is mapped to the true global time t by a function

$$T_n(t) = t + \epsilon_n(t) \tag{1}$$

where $\epsilon_n(t)$ is a time-varying bias that consists of a time-varying frequency offset random walk and a noise term consisting of thermal noise, shot noise, flicker noise, plasma noise, and quantum noise, among other sources, depending on device technology [21, chapter 10.1]. In this work, we assume that any time-varying frequency offset and the time offset $\delta_n(t)$ are quasi-static over the synchronization epoch; in the experiments discussed in this article, the systems are, furthermore, syntonized (synchronized in frequency) and, thus, over a long term, may be treated as a constant bias plus a noise term

$$\epsilon_n(t) = \delta_n(t) + \nu_n(t) \tag{2}$$

where $\delta_n(t)$ is the quasi-static time offset of node n relative to the global time during the synchronization epoch and $\nu_n(t)$ is the noise at node n at time t. The focus of this work is estimating and correcting for quasi-static bias term $\delta_n(t)$, which consists of static and dynamic components; dynamic components include frequency offset between platforms and time-varying internal delays caused by thermal expansion and nonlinear components whose propagation delay varies with environmental parameters; and static components include constant system delays due to trace and cable lengths internal to the system, which can be calibrated out. To simplify the model, it is assumed that node 0 is the true global time; thus, the bias of node zero is $\delta_0 = 0$, and the goal is to find $\Delta_{0n} = \delta_0 - \delta_n$.

B. Two-Way Time Transfer

In a two-way time transfer system, synchronization is achieved by sending a time delay estimation waveform between two nodes in both directions, schematically pictured in Fig. 2. Assuming that the link is quasi-static during the

synchronization epoch, the offset between the local clock at node n and node 0 can be deduced by

$$\Delta_{0n} = \frac{(t_{\text{RX}0} - t_{\text{TX}n}) - (t_{\text{RX}n} - t_{\text{TX}0})}{2}$$
 (3)

where t_{TXn} and t_{RXn} are the times of transmission and reception at node n, respectively. Once this offset is estimated, it may be added to the local clock at node n to compensate for the accumulated bias. Note that τ_{proc} , the processing time between the initial pulse reception at node n and its response, is arbitrary and does not affect the ability to determine the time offset so long as the assumption that the clock bias is quasi-static over the synchronization epoch is valid. Further clock characterization could be inferred by taking statistics over long-term bias correction to determine a constant drift between platforms, which could be tracked using techniques such as Kalman filtering to improve time stability between synchronization exchanges. If the link is symmetric, the propagation delay can also be deduced simply by

$$\tau_{0n} = \frac{(t_{\text{RX}0} - t_{\text{TX}n}) + (t_{\text{RX}n} - t_{\text{TX}0})}{2}.$$
 (4)

C. Theoretical Bounds on Time Delay Accuracy

The theoretical limit on the ability to accurately estimate the time delays in the above is dependent on the SNR and the waveform characteristics. The limit is given by the CRLB, which defines the variance on the estimate of the delay as [22, Ch. 7.2], [23]

$$\operatorname{var}(\hat{\tau} - \tau) \ge \frac{N_0}{2\zeta_f^2 E_s} \tag{5}$$

where ζ_f^2 is the mean-squared bandwidth (the second moment of the spectrum of the signal), E_s is the signal energy, and N_0 is the noise power spectral density (PSD), where

$$\frac{E_s}{N_0} = \tau_p \cdot \text{SNR} \cdot \text{NBW} \tag{6}$$

where τ_p is the pulse duration, SNR is the preprocessed SNR, and NBW is the noise bandwidth of the system. It is clear from (5) and (6) that the variance of the time delay estimate is inversely proportional to the SNR and mean-squared bandwidth of the waveform used. Thus, by increasing coherent integration time and transmission power, and mitigating channel and system noise, the variance of the time delay estimate may be reduced. However, of greater interest is designing a waveform, which maximizes the mean-squared bandwidth to obtain the highest accuracy theoretically possible for any given SNR level. In [23], it is shown that the mean-squared bandwidth for a waveform can be represented by

$$\zeta_f^2 = \int_{-\infty}^{\infty} (2\pi f)^2 |G(f)|^2 df \tag{7}$$

where G(f) is the PSD of the signal. From (7), it can be shown that concentrating the PSD of the waveform to the edges of the spectrum in a given bandwidth, yielding a two-tone waveform, maximizes the mean-squared bandwidth of the waveform, thus minimizing the estimation variance (5).

Computing the mean-squared bandwidth for a fully filled bandwidth waveform, such as the LFM, yields

$$\zeta_{f(\text{LFM})}^2 = \frac{(\pi \cdot \text{BW})^2}{3} \tag{8}$$

where BW is the maximum extent of the waveform bandwidth, whereas a two-tone waveform with its energy located at the edges of its bandwidth yields

$$\zeta_{f(\text{two-tone})}^2 = (\pi \cdot BW)^2 \tag{9}$$

an improvement by a factor of three. A waveform consisting of two tones at the edges of the spectrum is the optimal form of the time delay estimation waveform. This finding not only yields improved delay estimation but may also reduce system requirements as very large bandwidths can be synthesized using only two instantaneously narrowband transmitters as opposed to a single wideband transmitter, which are often very difficult to design and calibrate to ensure a uniform power response across the entire operating bandwidth. This channelized approach to two-tone high-accuracy delay estimation for range measurement was demonstrated experimentally in [24].

D. Time Delay Estimation and Refinement Process

To estimate the time delay of the received two-tone waveform, a matched filter is used, which maximizes the signal energy at the output of the filter at the time delay of the start of the received waveform. For a discretely sampled waveform, the matched filter output is

$$s_{\text{MF}}[n] = s_{\text{RX}}[n] \circledast s_{\text{TX}}^*[-n]$$

= $\mathcal{F}^{-1} \left\{ S_{\text{RX}} S_{\text{TX}}^* \right\}$ (10)

where $s_{\rm TX}$ is the ideal transmitted waveform, $s_{\rm RX}$ is the received waveform, and $(\cdot)^*$ is the complex conjugate [25], [26]. While a continuous-time matched filter maximizes the output power at the true time delay of the received waveform, the discrete-time matched filter produces a peak at the sample bin most closely corresponding to the true time delay of the received signal; this is an issue for high-accuracy time delay estimation as it implies that the estimation accuracy is limited by the sample rate of the digitizer. This may be overcome by increasing the sample rate, however, for high-accuracy requirements; this rapidly becomes prohibitively expensive using current hardware as sample rates exceed multiple gigahertz.

In contrast, a two-stage estimation can be employed where the coarse delay is estimated at the resolution of the data converter and then refined via processing to more accurately estimate the true time delay. One simple technique is quadratic least-squares (QLS) interpolation in which a parabola is fit to the peak of the matched filter and the two adjacent points; the time delay at the peak of the parabola is then regarded as the true time delay, graphically depicted in Fig. 3. The peak of a parabola formed by the peak of the discrete matched filter and its two adjacent sample points may be easily found in constant

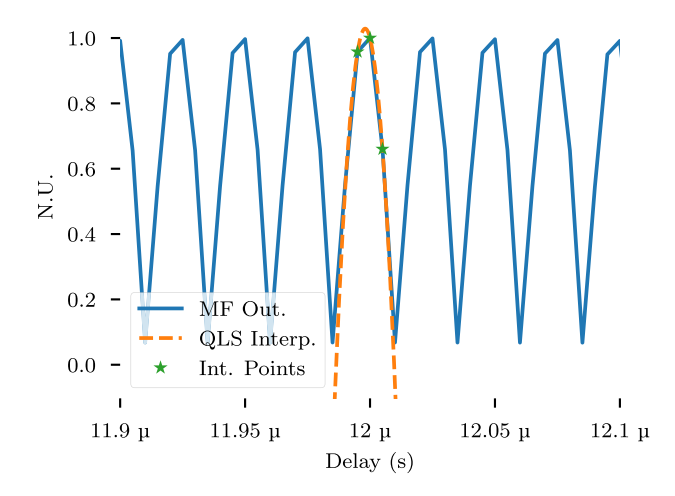


Fig. 3. Peak region of the discrete matched filter output for an ideal two-tone waveform (blue line). Quadratic least-squares (QLS) refinement (orange dashed line) is used to interpolate between sample points using the matched filter peak and two adjacent points (green dots) to mitigate discretization error

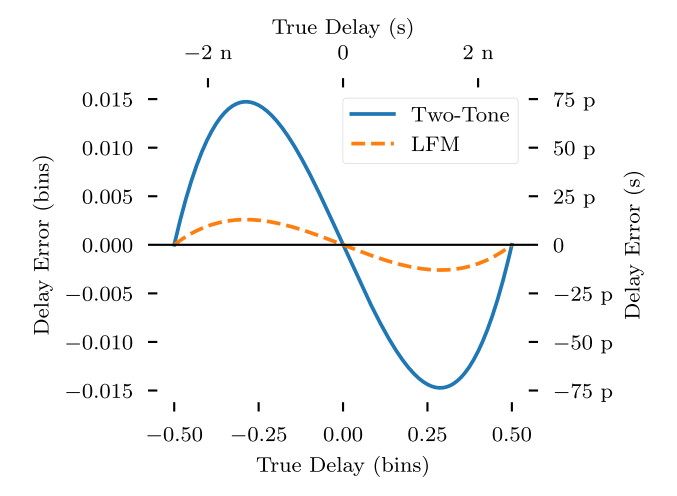


Fig. 4. Waveform and sample-rate dependent residual bias after QLS interpolation shown for 40-MHz two-tone and LFM waveforms. Given the cooperative nature of two-way time transfer, an LUT based on these curves may be used to correct for this bias by subtracting the bias at the given fractional true delay bin.

time complexity by [27], [22, Ch. 7.2]

$$n_{\text{max}} = \underset{n}{\operatorname{argmax}} \{s_{\text{MF}}[n]\}$$

$$\hat{\tau} = \frac{T_s}{2} \frac{s_{\text{MF}}[n_{\text{max}} - 1] - s_{\text{MF}}[n_{\text{max}} + 1]}{s_{\text{MF}}[n_{\text{max}} - 1] - 2 s_{\text{MF}}[n_{\text{max}}] + s_{\text{MF}}[n_{\text{max}} + 1]}$$
(12)

where T_s is the sampling interval.

QLS can greatly reduce the discretization errors introduced by the sample rate. However, if the underlying matched filter does not perfectly match a parabola, a residual delay-dependent bias will manifest in the intersample period $1/T_s$ that is inversely proportional to the QLS oversampling ratio, i.e., the factor by which the sampler exceeds the Nyquist frequency of the time delay waveform being sampled. The bias can be seen in Fig. 4 for the LFM and two-tone waveforms. It is also important to note that the shape of the bias is not

sinusoidal and is, furthermore, dependent on the waveform parameters. While the bias was present in both LFM and two-tone waveforms, the two-tone waveforms were found to have larger biases using this technique, e.g., for a two-tone waveform sampled at 200 MSa/s with a tone separation of 40 MHz, a peak bias of \sim 73 ps is expected, whereas an LFM of equal bandwidth exhibits a peak bias of only ~ 13 ps. as shown in Fig. 4. While these are large biases when working toward subpicosecond levels of precision, they are predictable if the waveform parameters and sample rates are known a priori and can be easily corrected via lookup table (LUT). By precomputing the expected biases at each fractional delay bin and storing the results in a LUT, the bias may be corrected for at runtime reducing the overall bias due to the estimator to arbitrarily low levels. Alternative peak interpolation techniques that more closely match the transmitted waveform include sinc nonlinear least-squares (sinc-LS) and matched filter leastsquares (MFLS) [26]. sinc-LS more closely approximates the shape of the output of the matched filter for two-tone signals but is an iterative approach and, thus, requires longer computation time than QLS. MFLS matches the shape of the output of the matched filter exactly but also requires the matched filter to be computed iteratively to optimize the fit of the estimated time delay proposal with the received signal, which requires significantly longer computation time than QLS. Due to the simplicity of implementation, low computational complexity, and relatively high accuracy achieved using QLS with a lookup table for bias correction, the QLS technique was chosen for use in these experiments.

It should also be noted that, while the systems are syntonized, the frequency jitter, captured by $v_n(t)$ in (2), will still impact the sampling uniformity of the analog-to-digital converter (ADC) and digital-to-analog converter (DAC) and, thus, cause distortion in the respective transmitted and received signals due to sampling nonuniformities; this will have the effect of reducing the accuracy of the matched filter due to distortion of the transmitted and sampled received waveforms resulting in a mismatch between the ideal and sampled waveforms.

III. FREQUENCY SYNCHRONIZATION

Frequency synchronization, or syntonization, is the process of making the clocks on all platforms resonate with the same period; this is essential for two reasons: 1) to ensure that the signals sum coherently at the destination and 2) to ensure that the transmitted and received waveforms are sampled with the same period to ensure that the matched filter correctly estimates the time delay of the received waveform for the time transfer and ranging estimation. If time synchronization is sufficiently accurate (i.e., a small fraction of the oscillator period) and is implemented with a sufficiently fast periodicity to minimize oscillator drift, the frequencies on each node can theoretically be synchronized directly by aligning the phases of the oscillators. However, not all systems have the ability to directly adjust the oscillator phase, particularly if time synchronization is added to existing legacy systems or commercial hardware. In these cases, frequency synchronization is

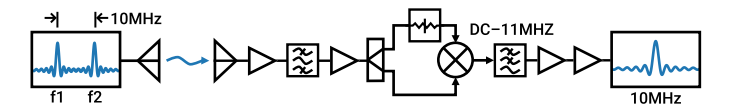


Fig. 5. Wireless frequency transfer circuit schematic. A two-tone waveform at the carrier frequency is transmitted with a tone separation of 10 MHz; the two-tone is received, amplified, and filtered and then split and self-mixed. The resultant signal consists of a 10-MHz tone with other tones near $2\,f_{0f}$, which are easily filtered by a low-pass filter. The 10-MHz tone is, finally, amplified by a clock buffer to produce a 10-MHz square wave for frequency reference to the SDP

also necessary and may allow for a relatively infrequent time synchronization interval.

There are many ways to accomplish wireless frequency synchronization, which broadly fall into three categories: closed-loop, open-loop centralized, and open-loop decentralized. In a closed-loop topology, the distributed nodes utilize feedback from a cooperative target, which transmits back information used to tune the distributed nodes to the proper transmit frequency [28], [29]. While this can be useful in communication systems, for targets with passive receivers or radar applications, nodes cannot rely on feedback from a target and must implement open-loop topologies. In an open-loop centralized architecture, a single primary node is utilized as the "leader" that generates the frequency reference for all other nodes to syntonize to [30], [31], [32]. This approach enables remote observation and communications with passive targets but has a single point of failure at the primary node and inherently has an array size limit due to increasing path loss between the primary node and followers as the array size grows. Finally, the open-loop distributed architecture consists of many nodes that all perform a frequency consensus averaging operation, wherein all nodes in the array attempt to estimate the frequency of all other adjacent nodes and adjust their own frequency to the average of the estimates [33], [34], [35]. This approach is the most robust to interference and avoids the single point of failure and scaling difficulties of the open-loop centralized architecture; however, it is also the most difficult to implement due to the necessity of separately estimating and tracking the frequencies from multiple nodes and performing online adjustment of the local carrier frequency, which typically requires a softwarebased implementation.

In this article, we implement an open-loop centralized approach due to its balance of being able to perform radar and passive target communication operations, as well as being relatively simple to implement in a hardware circuit. A spectrally sparse technique using a self-mixing receiver is utilized [32], [36] to provide improved robustness compared to single-tone frequency transfer techniques, which are more susceptible to external interference. The principle of operation is shown in Fig. 5. A two-tone waveform with a tone separation of $\beta_f = 10$ MHz is generated at an arbitrary carrier frequency f_{0f} , the tones are received at the self-mixing circuit where out-of-band noise is filtered by a bandpass filter, and the signal is amplified and mixed with itself. This generates tones at the sum and difference of the original received tones resulting in a 10-MHz tone and other tones around $2 f_{0f}$, the latter of which is

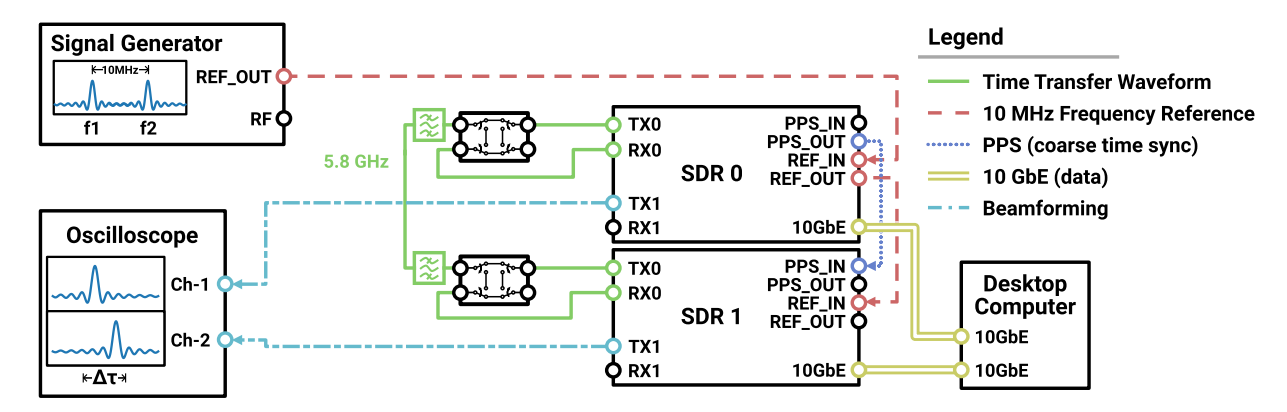


Fig. 6. Fully cabled time–frequency transfer system schematic. The signal generator is used as the primary frequency reference for SDR 0 (primary SDR), which provides the frequency reference for SDR 1 (secondary SDR). The oscilloscope is used to sample and digitize the beamforming waveforms to determine beamforming accuracy while performing time transfer. Control transfer switches were used to provide high isolation between transmit and receive paths during time-domain multiplexing operation. Both SDRs were controlled by a single desktop computer using GNU Radio during operation. A pulse-per-second (PPS) signal was used on device startup for an initial, coarse time alignment to ensure transmit and receive windows on each SDR overlap for the fine time alignment process to proceed. Unused ports on switches were terminated with matched loads.

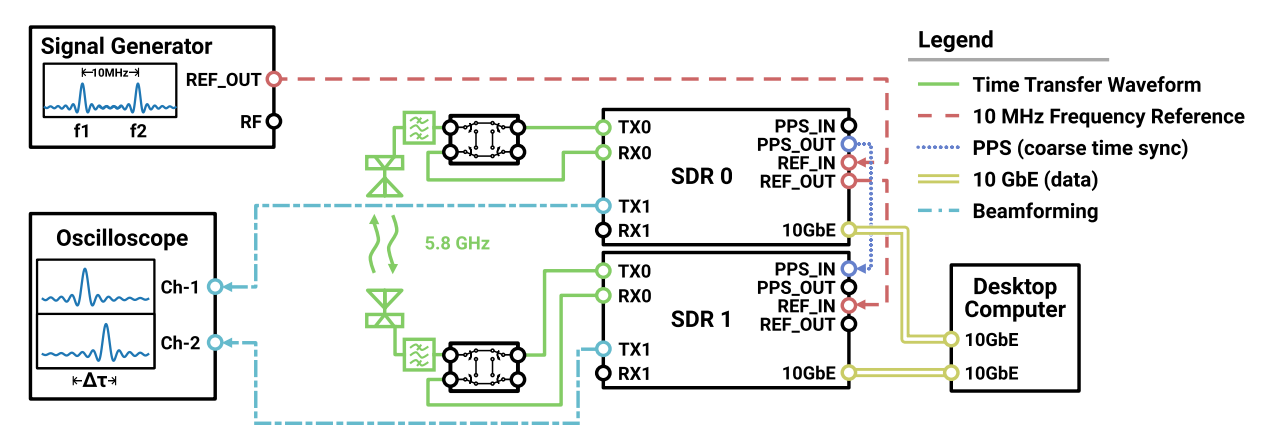


Fig. 7. Wireless time transfer, cabled frequency syntonization system schematic. The experiment was configured similar to the fully cabled experiment with the exception that time transfer was performed over a wireless link. Unused ports on switches and splitters were terminated with matched loads.

easily removed by a low-pass filter. Finally, the 10-MHz tone is converted to a square wave via a clock amplifier to provide optimal performance for the frequency reference on the SDR. It should be noted that the tone separation β_f is chosen to be 10 MHz due to the requirement of a 10-MHz reference input on the SDRs; however, this may be any arbitrary value that is advantageous for the device requiring a frequency reference.

Finally, while, in these experiments, we use separate radio frequency (RF) bands for the time and frequency transfer waveforms, there is no specific requirement for the waveforms to exist in any given band since the performance is strictly bandwidth-dependent. Furthermore, it has previously been shown that these two functions can coexist in the same band: in [37], a three-tone waveform was used to accomplish frequency transfer and ranging using a narrow tone separation of 10 MHz for frequency transfer and a wide tone separation of 200 MHz for range (time delay) estimation. This could be employed for time–frequency transfer as well by simply pulsing the time transfer tone while keeping the two frequency transfer tones' continuous wave; however, it was chosen to use separate RF bands for this experiment for simplicity.

IV. HIGH-PRECISION TIME TRANSFER EXPERIMENTS

A. Experimental Configuration

The time transfer experiments consisted of three configurations:

- 1) fully cabled time-frequency transfer (see Fig. 6);
- 2) wireless time transfer with cabled frequency syntonization (see Fig. 7);
- 3) fully wireless time–frequency transfer (see Fig. 8).

Each of the experiments was repeated with SNRs varying from 6 to 36 dB in 3-dB increments; at each SNR level, the precision of the time-transfer waveform and beamforming waveforms was recorded. An additional sweep of tone separation was included for the fully cabled time–frequency transfer experiment to validate the accuracy trends for varying tone separations relative to the CRLB, while the preprocessing SNR was held at 30 dB.

System schematics for each of the experiments are shown in Figs. 6–8, and the experimental setups for the wired and wireless configurations are pictured in Figs. 9 and 10, respectively. A summary of the experimental parameters is provided in Table I. The SDRs used in these experiments were

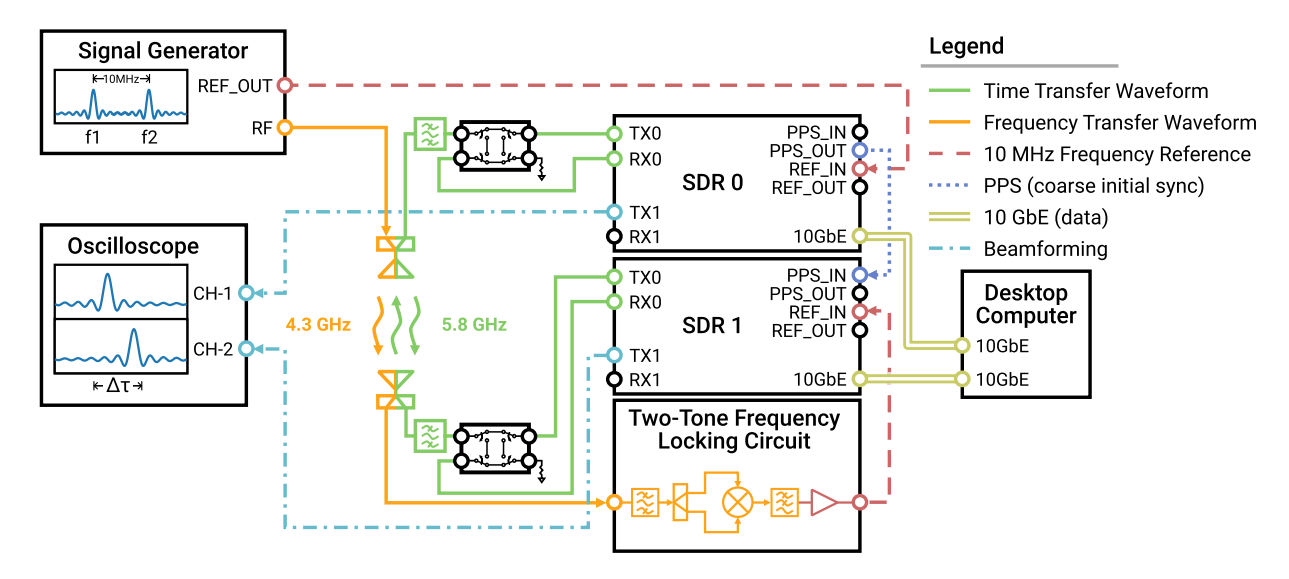


Fig. 8. Fully wireless time-frequency transfer system schematic. The experiment was configured similar to the wireless time transfer experiment; however, the signal generator was used the two-tone generator for the self-mixing frequency locking circuit, used as the frequency reference for SDR 1 (secondary SDR). Unused ports on switches and splitters were terminated with matched loads.

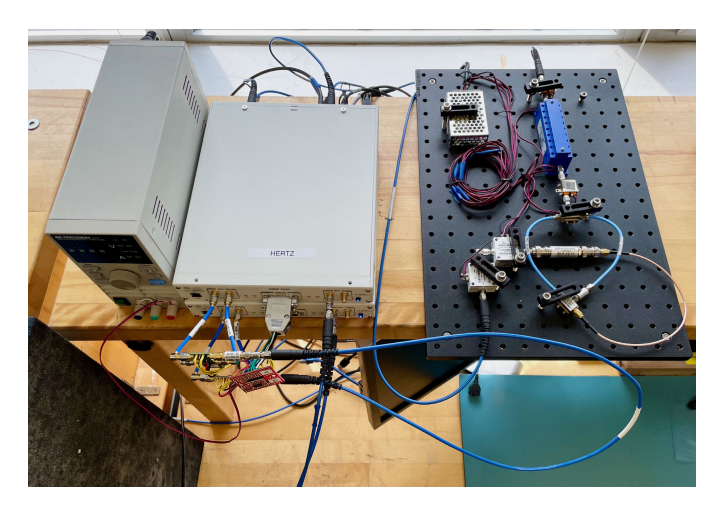


Fig. 9. Detail image of the SDRs in the fully cabled configuration (left) with the two-tone self-mixing frequency locking circuit (right).

Ettus Research Universal Software Radio Peripheral (USRP) X310's each equipped with two UBX-160 daughterboards that provided 160 MHz of instantaneous analog bandwidth; the X310s were run with a base clock of 200 MHz and a digital sampling rate of 200 MSa/s. To provide high isolation between the transmit and receive paths, two Analog Devices (ADI) HMC427A control transfer switches were used and controlled using the general-purpose input/output (GPIO) pins on the SDRs. Finally, each SDR used a bandpass filter to separate the 4.3-GHz frequency-transfer tones from the 5.8-GHz time transfer tones, reducing the distortion of the received signals. A pulse-per-second (PPS) cable was connected between SDRs for a coarse initial time alignment and is only used once on initialization; this aligned the systems to within several clock ticks, which is required to align the finite transmit and receive windows close enough that the time synchronization pulses transmitted would arrive within the receive window. This coarse time alignment could also be achieved fully

TABLE I
EXPERIMENT PARAMETERS

Time Transfer Waveform				
Parameter	Symbol	Value		
Waveform Type		Pulsed Two-Tone		
Carrier Frequency	$f_{ m Ot}$	$5.8\mathrm{GHz}$		
Tone Separation	$eta_{ m t}$	$40\mathrm{MHz}$		
Rise/Fall Time		$50\mathrm{ns}$		
Pulse Duration	$ au_{ m p}$	$10.0\mathrm{\mu s}$		
Synchronization Epoch Duration	•	$50.01\mathrm{ms}$		
Resynchronization Interval		$100.0\mathrm{ms}$		
Rx Sample Rate	$f_{ m s_}^{ m Rx}$	$200\mathrm{MSa/s}$		
Tx Sample Rate	$f_{ m s}^{ m Tx}$	$400\mathrm{MSa/s}^*$		

Frequency Transfer Waveform

Parameter	Symbol	Value	
Waveform Type		CW Two-Tone	
Carrier Frequency	$f_{ m Of}$	$4.3\mathrm{GHz}$	
Tone Separation	$eta_{ m f}$	$10\mathrm{MHz}$	

Beamforming Waveform

Parameter	Symbol	Value	
Waveform Type		Pulsed Two-Tone	
Carrier Frequency	$f_{ m Ob}$	$1.2\mathrm{GHz}$	
Tone Separation	$eta_{ m b}$	$50\mathrm{MHz}$	
Rise/Fall Time		$50\mathrm{ns}$	
Pulse Duration	$ au_{ m D}$	$10.0\mu\mathrm{s}$	
Tx Sample Rate	$f_{ m s}^{ m Tx}$	$400\mathrm{MSa/s}^*$	
Rx Sample Rate	$f_{ m s}^{ m osc}$	$20\mathrm{GSa/s}$	

Antenna Parameters

Parameter	Symbol	Value
Gain Bandwidth Separation (radome-to-radome)		8 dBi 2.3–6.5 GHz 90 cm

^{*} Digitally upsampled from 200 MSa/s to 400 MSa/s on device

wirelessly by first starting at a low sampling rate and using low bandwidth waveforms with either continuously streaming receivers or large receive time windows to obtain a coarse



Fig. 10. Wireless configuration experimental setup. Signal generator (left) used for the primary SDR's (SDR 0) frequency reference for all experiments and two-tone generation in the fully wireless time–frequency transfer experiment. Time and frequency transfer antennas (center), oscilloscope, SDRs, and control computer (right).

inter-SDR time offset while accommodating the processing power of the host computer; shorter receive windows could be used with progressively higher sample rates to refine the time delay estimate until the full bandwidth of the device is realized, if needed. Other more conventional approaches may also be used, such as GNSS PPS synchronization or adjunct ultrawideband (UWB) transmitters if the application permits. For the fully cabled time-frequency transfer and cabled frequency syntonization experiments, the 10-MHz reference output of SDR 0 was connected directly to the reference input of SDR 1, and for the fully cabled experiment, the time transfer was performed over a 3-ft coaxial cable with a 30-dB attenuator, as shown in Fig. 9. During the wireless experiments, two L-Com 8-dBi 2.3–6.5-GHz log-periodic antennas were placed 90 cm apart (radome to radome) to perform the time and frequency transfer, as shown in Fig. 10.

A Keysight PSG E8267D vector signal generator was used to generate the 10-MHz frequency reference for SDR 0 for all experiments and generate the two-tone waveform with a 4.295-GHz carrier tone and a single 4.305-GHz sideband used by the self-mixing frequency locking circuit (see Fig. 9 [32, Section II]) to generate the 10-MHz reference for SDR 1 in the fully wireless experiment; for all other experiments, SDR 1 was locked to the 10-MHz reference output of SDR 0. In all experiments, a Keysight DSOS804A 20 GSa/s oscilloscope configured with an 8.4-GHz analog bandwidth was used to capture the two beamforming waveforms for pulse alignment estimation.

To control and process the data from the SDRs, each SDR was connected to a desktop computer using 10-Gbit Ethernet. The control and processing computer consisted of a 2.3-GHz Intel i5-2500T processor with 32 GB of 1333-MHz DDR3 memory running Ubuntu 20.04. GNU Radio 3.9 and the Ettus Universal Software Radio Peripheral (USRP) Hardware Driver (UHD) 4.1 were used to interface with the SDRs and process the data in real time. To achieve the full 200-MSa/s performance and ensure the most accurate timing, the SDRs were programmed for bursty operation using timed transmissions/receptions, which allowed scheduling of messages to be transmitted and received down to a single local clock tick on each platform. However, due to API limitations at the time of implementation, an in-place local clock update

operation was not supported, so local time offsets were stored on the control computer and manually added to the scheduled transmit times to ensure that clocks were aligned in the software. The clocks were aligned using the two-way time synchronization exchange, as described in Section II-B, with a pulse repetition interval (PRI) of 50 ms, a pulse duration of 10 μ s, and a two-tone bandwidth of 40 MHz. Each time delay was estimated using a single waveform pulse. A finite rise and fall time of 50 ns was applied to the time transfer waveform envelope to generate a waveform, which could more realistically be generated by the device with finite switching time and, thus, generate a signal, which is closer to the ideal signal used for matched filtering. Furthermore, by spreading the rising edge of the envelope across several samples, the exact time of arrival between sample bins can be more easily deduced due to the addition of waveform amplitude modulation.

To determine the accuracy of the secondary beamforming channel with high precision, 50-MHz 1-µs two-tone waveforms with a 1.2-GHz carrier frequency were used. A two-tone waveform was used for the beamforming signal rather than a typical communications or radar waveform because, as described in Section II-C, the two-tone waveform provides the optimal accuracy in measuring the timing accuracy of the beamformed signals. A 1.2-GHz carrier was chosen for its minimal phase noise on the UBX-160 daughterboards. The signals were digitized by the oscilloscope and saved to disk and digitally downconverted and cross-correlated in postprocessing using Python to determine their interarrival time difference. The standard deviation was then computed for each SNR; the long-term bias trends were also measured for the maximum SNR case of 36 dB. The time-transfer stability was measured using the standard deviation of the self-reported timing corrections based on the two-way time transfer process.

To perform the SNR control, the transmit gain was first increased until reaching a gain of 30 dB (~+15 dBm) at which point the receive gain was increased to reach an estimated SNR of 36 dB. To estimate the SNR, a simple root mean square (rms) power method was used. Because both the two-tone and LFM waveforms are constant-amplitude pulses, the rms signal power could be determined directly from the measured signal

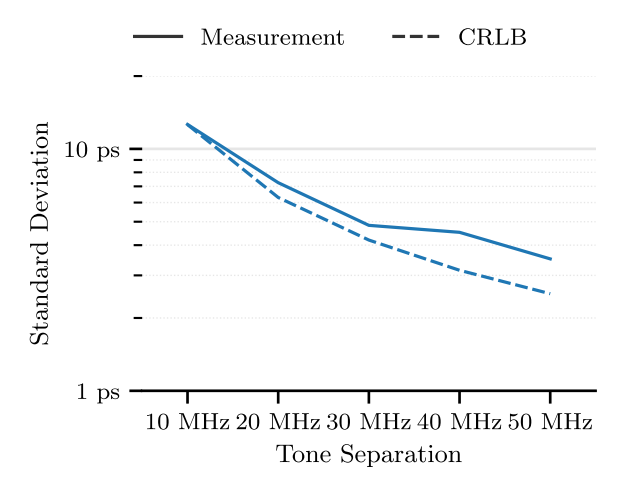


Fig. 11. Accuracy versus tone separation relative to the CRLB for the pulsed two-tone time transfer process when fully cabled. The tone separation was varied from 10–50 MHz, and measurements were collected at a preprocessing SNR of 30 dB at a carrier of $f_{0t} = 5.8$ GHz.

envelope in a $50-\Omega$ system by

$$P_s = \sqrt{\frac{1}{N} \sum_{n=1}^{N} \frac{|r_s[n]|^2}{50}}$$
 (13)

where N is the number of samples received and r_s is the received pulse samples. The noise power was similarly estimated from the received signal envelope when there was no transmission occurring by

$$P_n = \sqrt{\frac{1}{N} \sum_{n=1}^{N} \frac{|r_n[n]|^2}{50}}$$
 (14)

where r_n is the received signal when there was no transmission occurring; an equal number of noise samples were used to calculate the noise power. Finally, the SNR was estimated by

$$SNR = 10 \log_{10} \left[\left(\frac{P_s}{P_n} \right)^2 \right]. \tag{15}$$

B. Experimental Results

During each of these experiments, the synchronization epoch occurred over 50-ms intervals and resynchronized every 50 ms. Utilizing these parameters, the system precision (standard deviation) and accuracy (standard deviation + bias) were collected. The precision was measured over a range of SNRs using 1000 beamforming pulses over approximately 2 min, the results of which are shown in Figs. 11 and 12 for the bandwidth/tone separation sweep and SNR sweeps, respectively. In Fig. 11, the measured time transfer accuracy is shown in a solid line, while the CRLB is shown as a dashed line; for both the two-tone and LFM, the measured data follow the trend of the CRLB; however, the two-tone approaches more closely to the CRLB. The time transfer accuracy is denoted in Fig. 12 in solid blue, while the beamforming accuracy, computed from the cross-correlated oscilloscope samples, is shown as a dashed blue line. For moderate to high SNRs of >15 dB, the beamforming accuracy is typically \sim 3 ps higher than the time alignment accuracy. Furthermore, it is noted that the experiment using the fully wireless two-tone time-frequency transfer circuit, as summarized in Fig. 12(c), imposes a lower bound on the time transfer precision of \sim 10 ps past 15-dB SNR due to an increased clock phase noise from the frequency transfer circuit. However, the wireless time transfer technique alone using cabled frequency syntonization closely follows that of the fully cabled time-frequency transfer case demonstrating the efficacy of the technique over wireless links.

The long-term bias between the information beamforming channels on each SDR was also taken over multiple 1500-s periods across multiple days to demonstrate the typical biases experienced, the results of which are shown in Fig. 13. The biases consist of a static offset and a small slowly time-varying bias. Factors that contribute to the initial bias are initial PPS triggering latency, internal device delays, constant interchannel timing skew, and external transmission line length mismatch between the SDR and oscilloscope. This static bias can be calibrated out by measuring the average interchannel bias over a short period such that the minimal time-varying drift occurs, then switching the channels that the cables are connected to on the SDR and repeating the process, and then averaging the results of the two measurements to remove any variation in cable and adapter length, and oscilloscope input circuitry. The small slowly time-varying bias typically varies by <100 ps over long durations (hours to days), which is believed to be due to a small time-varying interchannel timing skew internal to each SDR, which causes the sampled signals on each channel, and each data converter within each channel, to be sampled with a slight, relative time-varying skew; these small timing skews are cumulative and can sum to cause the ~ 100 -ps skews observed. Because of this, the long-term accuracy is limited by the interdevice timing skews specific to the device used in this experiment.

C. Discussion

As discussed in Section IV-B, the total accuracy is limited by the slowly time-varying interchannel hardware bias; if left uncorrected, this could reduce the overall system beamforming bandwidth. However, this could be corrected in a similar way to the intersystem time transfer process by periodically performing an intrasystem time transfer operation to remove the self-bias between channels. It should also be noted that an online optimization system could be utilized to determine the optimal times to perform clock updates based on overall system drift characterization. In this article, we demonstrate a constant periodic synchronization; however, if the system is static with well-syntonized clocks, it may be beneficial to reduce the resynchronization frequency to avoid jitter in the timing. This could be implemented by periodically checking for interdevice timing skew and allowing a time-offset correction only when it is outside the tolerable limits. This would reduce the overall beamforming jitter in cases where the inter-SDR bias is smaller than the precision of the time transfer link, e.g., in low-SNR environments or when very high-quality oscillators are used, while still maintaining a high level of timing coherence between the systems. In addition, as described in the CRLB given by (5) and (6), and verified

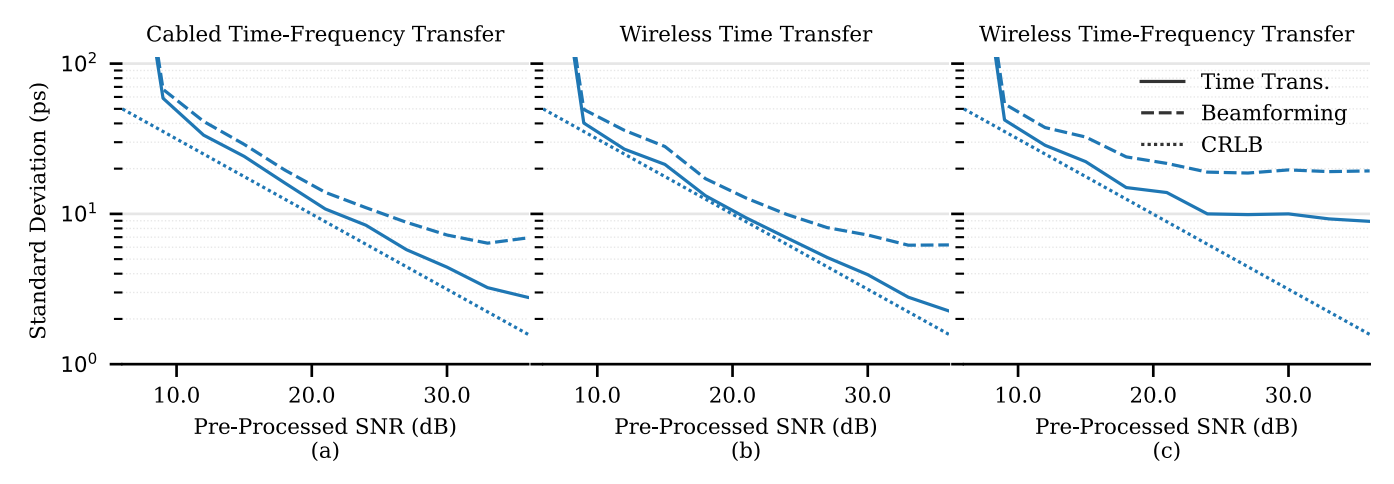


Fig. 12. Precision measurements ranging from 6–36-dB SNR for each of (a) cabled time–frequency transfer, (b) wireless time transfer, and (c) wireless time–frequency transfer experiments. The time transfer measurement is the self-reported standard deviation of the time synchronization between SDRs; the beamforming measurements is the standard deviation of the beamforming pulses set to the oscilloscope; and the CRLB is the theoretical lower bound computed using (5)–(9). The CRLB is presented for the "best case" SNR within the SNR estimate uncertainty of ± 3 dB.

TABLE II

Comparison of Current Subnanosecond Microwave and Millimeter-Wave Wireless Time Transfer Technique Stability

Reference	Waveform*	SNR (dB)	Carrier Frequency (GHz)	Bandwidth (MHz)	Standard Deviation (ps)	Figure of Merit [†] (Lower is better)
[38]	802.15.4 UWB (D)	NA	3.5-6.5	~900	477	\sim 429, 300
[14]	802.11n (D)	NA	2.412	20	~650	~13,000
[39]	LFM	NA	5.725	150	66	9,900
[40]	LFM	NA	3.120	40	< 100	< 4,000
[12]	White Rabbit (D)	NA	72.0–75.0	1,600	< 2.0	< 3,200
[13]	LFM	31.2	1.0	50	11.3	565
This Work	Two-Tone	30.0	5.8	40	3.94	157.6
This Work	Two-Tone	36.0	5.8	40	2.26	90.4

^{*(}D) = digitally modulated waveform

NA: Not available at time of publication

experimentally, the accuracy of the time delay estimate is improved by increasing SNR; the SNR of the system may be increased by means of increasing transmit power or reducing system noise; however, these gains become significantly more difficult at higher SNR.

Finally, a comparison of the results in this work to other similar microwave and millimeter-wave wireless time transfer systems is shown in Table II. An figure of merit (FoM) to rank the achieved system time transfer precision versus the occupied signal bandwidth is defined as the product of the signal bandwidth in MHz and the time transfer standard deviation in picoseconds; thus, a lower FoM indicates better timing performance with a lower signal bandwidth. We chose this FoM because it captures the controllable aspect of the waveform (the bandwidth) along with the performance (the time synchronization standard deviation). While an alternative metric may include the SNR, very few other works in the literature report this value. The time transfer approach demonstrated in this work yielded an FoM of 90.4 with an SNR of 36 dB and 157.6 with an SNR of 30 dB. This SNR value is

comparable to one other work that reported SNR [13], which had an SNR of 31.2 dB but which achieved an FoM of 565, far higher than that reported in this work. It is important to note that all other waveforms used in time transfer works in the literature were filled bandwidth waveforms, such as LFMs [13], [39], [40] and digitally encoded waveforms [12], [14], [38]. In contrast, in our approach, the waveform uses only two tones at the ends of the bandwidth; thus, the bandwidth between the tones can be left unused to reduce bandwidth requirements on the system by implementing only two narrowband signal generators to produce the two-tone pulses, or it can be used for other wireless operations, such as coarse PPS or internode communications; this is not possible with other filled-bandwidth waveforms. While the performance to spectral efficiency of the two-tone time transfer method is significantly greater than the other conventional filled bandwidth techniques listed, it should be noted that the accuracy of some of the other works was evaluated outside of laboratory environments, which may reduce accuracy due to multipath and uncontrollable environmental dynamics. Using this method,

[†] Figure of merit (FoM) = bandwidth (MHz) \times standard deviation (ps)

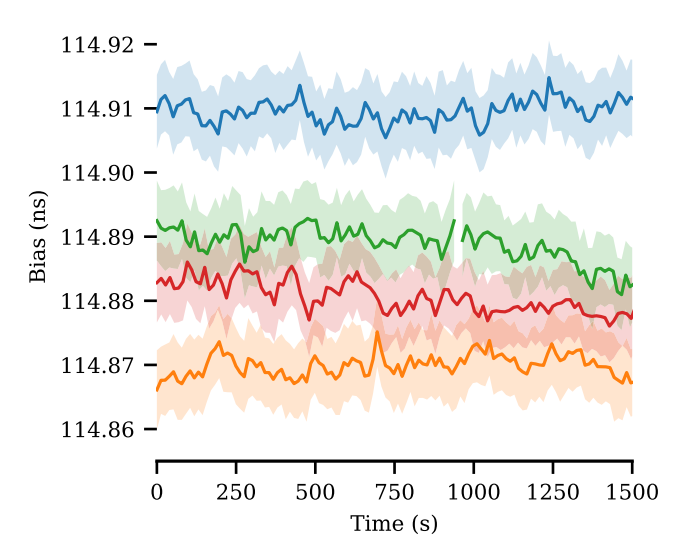


Fig. 13. Long-term beamforming bias trends taken across multiple days without constant bias removed. The shaded region depicts one standard deviation. Constant bias of $\sim\!114.89$ ns due to initial PPS triggering latency, internal SDR delays, and external transmission line mismatch; slowly time-varying bias of $<\!100$ ps believed to be due to a time-varying internal SDR clock distribution skew.

it is clear that the two-tone time transfer waveform provides a bandwidth-efficient technique for achieving high-accuracy wireless time transfer in distributed wireless systems.

V. CONCLUSION

In this article, we demonstrated the first fully wireless time transfer system capable of synchronizing time between two systems to a precision of 2.26 ps over a 36-dB SNR wireless link using a novel single-pulse two-tone time delay estimation technique, which achieves the highest known theoretical accuracy for a given signal bandwidth. This shows a significant step toward improving the overall system accuracy toward subpicosecond timing alignment using RF systems enabling high-accuracy coordination in wireless distributed arrays for high bandwidth distributed antenna arrays.

REFERENCES

- 2020 NASA Technology Taxonomy, Nat. Aeronaut. Space Admin., Washington, DC, USA, Jan. 2020.
- [2] 2015 NASA Technology Roadmaps, Nat. Aeronaut. Space Admin., Washington, DC, USA, Jul. 2015.
- [3] D. Tagliaferri et al., "Cooperative synthetic aperture radar in an urban connected car scenario," in *Proc. 1st IEEE Int. Online Symp. Joint Commun. Sens. (JC&S)*, Feb. 2021, pp. 1–4.
- [4] J. A. Nanzer, S. R. Mghabghab, S. M. Ellison, and A. Schlegel, "Distributed phased arrays: Challenges and recent advances," *IEEE Trans. Microw. Theory Techn.*, vol. 69, no. 11, pp. 4893–4907, Nov. 2021.
- [5] J. A. Nanzer, R. L. Schmid, T. M. Comberiate, and J. E. Hodkin, "Open-loop coherent distributed arrays," *IEEE Trans. Microw. Theory Techn.*, vol. 65, no. 5, pp. 1662–1672, May 2017.
- [6] F. R. Giorgetta et al., "Optical two-way time and frequency transfer over free space," *Nature Photon.*, vol. 7, pp. 434–438, Apr. 2013.
- [7] L. C. Sinclair et al., "Synchronization of clocks through 12 km of strongly turbulent air over a city," *Appl. Phys. Lett.*, vol. 109, no. 15, 2016, Art. no. 151104.
- [8] L. C. Sinclair et al., "Femtosecond optical two-way time-frequency transfer in the presence of motion," *Phys. Rev. A, Gen. Phys.*, vol. 99, no. 2, 2019, Art. no. 023844.

- [9] M. L. Sichitiu and C. Veerarittiphan, "Simple, accurate time synchronization for wireless sensor networks," in *Proc. IEEE Wireless Commun. Netw. Conf. (WCNC)*, vol. 2. Mar. 2003, pp. 1266–1273.
- [10] S. Ganeriwal, R. Kumar, and M. B. Srivastava, "Timing-sync protocol for sensor networks," in *Proc. 1st Int. Conf. Embedded Networked Sensor* Syst., 2003, pp. 138–149.
- [11] J. Hill and D. Culler, "A wireless embedded sensor architecture for system-level optimization," Dept. Elect. Eng. Comput. Sci., Univ. California, Berkeley, Berkeley, CA, USA, Tech. Rep., 2002.
- [12] J. E. Gilligan, E. M. Konitzer, E. Siman-Tov, J. W. Zobel, and E. J. Adles, "White rabbit time and frequency transfer over wireless millimeter-wave carriers," *IEEE Trans. Ultrason.*, Ferroelectr., Freq. Control, vol. 67, no. 9, pp. 1946–1952, Sep. 2020.
- [13] S. Prager, M. S. Haynes, and M. Moghaddam, "Wireless subnanosecond RF synchronization for distributed ultrawideband software-defined radar networks," *IEEE Trans. Microw. Theory Techn.*, vol. 68, no. 11, pp. 4787–4804, Nov. 2020.
- [14] O. Seijo, J. A. Lopez-Fernandez, H.-P. Bernhard, and I. Val, "Enhanced timestamping method for subnanosecond time synchronization in IEEE 802.11 over WLAN standard conditions," *IEEE Trans. Ind. Informat.*, vol. 16, no. 9, pp. 5792–5805, Sep. 2020.
- [15] J. M. Merlo and J. A. Nanzer, "High accuracy wireless time synchronization for distributed antenna arrays," in *Proc. IEEE Int. Symp. Anten*nas Propag. USNC-URSI Radio Sci. Meeting (AP-S/URSI), Jul. 2022, pp. 1966–1967.
- [16] J. Levine, "A review of time and frequency transfer methods," *Metrologia*, vol. 45, no. 6, pp. S162–S174, Dec. 2008.
- [17] R. S. Cooper and A. R. Chi, "A review of satellite time transfer technology: Accomplishments and future applications," *Radio Sci.*, vol. 14, no. 4, pp. 605–619, Jul. 1979.
- [18] D. W. Hanson, "Fundamentals of two-way time transfers by satellite," in Proc. 43rd Annu. Symp. Freq. Control, May 1889, pp. 174–178.
- [19] D. Kirchner, "Two-way time transfer via communication satellites," Proc. IEEE, vol. 79, no. 7, pp. 983–990, Jul. 1991.
- [20] J. Serrano et al., "The white rabbit project," in Proc. IBIC, 2013, pp. 936–942.
- [21] D. Pozar, Microwave Engineering, 3rd ed. Hoboken, NJ, USA: Wiley, 2005.
- [22] M. Richards, Fundamentals of Radar Signal Processing, 2nd ed. New York, NY, USA: McGraw-Hill, 2014.
- [23] J. A. Nanzer and M. D. Sharp, "On the estimation of angle rate in radar," *IEEE Trans. Antennas Propag.*, vol. 65, no. 3, pp. 1339–1348, Mar. 2017.
- [24] A. Schlegel, S. M. Ellison, and J. A. Nanzer, "A microwave sensor with submillimeter range accuracy using spectrally sparse signals," *IEEE Microw. Wireless Compon. Lett.*, vol. 30, no. 1, pp. 120–123, Jan. 2020.
- [25] M. Richards, W. Holm, and J. Scheer, *Principles of Modern Radar: Basic Principles* (Electromagnetics and Radar), vol. 1. Edison, NJ, USA: IET, 2010.
- [26] S. R. Mghabghab and J. A. Nanzer, "Microwave ranging via least-squares estimation of spectrally sparse signals in software-defined radio," *IEEE Microw. Wireless Compon. Lett.*, vol. 32, no. 2, pp. 161–164, Feb. 2022
- [27] R. Moddemeijer, "On the determination of the position of extrema of sampled correlators," *IEEE Trans. Signal Process.*, vol. 39, no. 1, pp. 216–219, Jan. 1991.
- [28] M. Seo, M. Rodwell, and U. Madhow, "A feedback-based distributed phased array technique and its application to 60-GHz wireless sensor network," in *IEEE MTT-S Int. Microw. Symp. Dig.*, Jun. 2008, pp. 683–686.
- [29] P. Bidigare et al., "Implementation and demonstration of receiver-coordinated distributed transmit beamforming across an ad-hoc radio network," in *Proc. Conf. Rec. 46th Asilomar Conf. Signals, Syst. Comput.* (ASILOMAR), 2012, pp. 222–226.
- [30] G. Barriac, R. Mudumbai, and U. Madhow, "Distributed beamforming for information transfer in sensor networks," in *Proc. 3rd Int. Symp. Inf. Process. Sensor Netw.*, 2004, pp. 81–88.
- [31] D. R. Brown, G. B. Prince, and J. A. McNeill, "A method for carrier frequency and phase synchronization of two autonomous cooperative transmitters," in *Proc. IEEE 6th Workshop Signal Process. Adv. Wireless Commun.*, 2005, pp. 260–264.
- [32] S. R. Mghabghab and J. A. Nanzer, "Open-loop distributed beamforming using wireless frequency synchronization," *IEEE Trans. Microw. Theory Techn.*, vol. 69, no. 1, pp. 896–905, Jan. 2021.
- [33] H. Ouassal, T. Rocco, M. Yan, and J. A. Nanzer, "Decentralized frequency synchronization in distributed antenna arrays with quantized frequency states and directed communications," *IEEE Trans. Antennas Propag.*, vol. 68, no. 7, pp. 5280–5288, Jul. 2020.

- [34] H. Ouassal, M. Yan, and J. A. Nanzer, "Decentralized frequency alignment for collaborative beamforming in distributed phased arrays," *IEEE Trans. Wireless Commun.*, vol. 20, no. 10, pp. 6269–6281, Oct. 2021.
- [35] M. Rashid and J. A. Nanzer, "Frequency and phase synchronization in distributed antenna arrays based on consensus averaging and Kalman filtering," 2022, arXiv:2201.08931.
- [36] O. Abari, H. Rahul, D. Katabi, and M. Pant, "AirShare: Distributed coherent transmission made seamless," in *Proc. IEEE Conf. Comput. Commun. (INFOCOM)*, Apr. 2015, pp. 1742–1750.
- [37] S. M. Ellison, S. Mghabghab, J. J. Doroshewitz, and J. A. Nanzer, "Combined wireless ranging and frequency transfer for internode coordination in open-loop coherent distributed antenna arrays," *IEEE Trans. Microw. Theory Techn.*, vol. 68, no. 1, pp. 277–287, Jan. 2020.
- [38] K. Alemdar, D. Varshney, S. Mohanti, U. Muncuk, and K. Chowdhury, "RFClock: Timing, phase and frequency synchronization for distributed wireless networks," in *Proc. 27th Annu. Int. Conf. Mobile Comput. Netw.*, Sep. 2021, pp. 15–27.
- [39] S. Roehr, P. Gulden, and M. Vossiek, "Method for high precision clock synchronization in wireless systems with application to radio navigation," in *Proc. IEEE Radio Wireless Symp.*, Jan. 2007, pp. 551–554.
- [40] R. K. Pooler, J. S. Sunderlin, R. H. Tillman, and R. L. Schmid, "A precise RF time transfer method for coherent distributed system applications," in *Proc. USNC-URSI Radio Sci. Meeting*, Jul. 2018, pp. 5–6.



Jason M. Merlo (Graduate Student Member, IEEE) received the B.S. degree in computer engineering from Michigan State University, East Lansing, MI, USA, in 2018, where he is currently pursuing the Ph.D. degree in electrical engineering.

From 2017 to 2021, he was a Project Manager and the Electrical Systems Team Lead of the Michigan State University AutoDrive Challenge Team. His current research interests include distributed radar and wireless system synchronization, interferometric arrays, synthetic aperture radar, joint radar commu-

nications, and automotive/automated vehicle radar applications.



Serge R. Mghabghab (Member, IEEE) received the B.E. degree in electrical engineering from Notre Dame University—Louaize, Zouk Mosbeh, Lebanon, in 2014, the M.E. degree in electrical and computer engineering from the American University of Beirut, Beirut, Lebanon, in 2017, and the Ph.D. degree in electrical engineering from Michigan State University, East Lansing, MI, USA, in 2022.

In 2022, he joined MathWorks, Natick, MA, USA.



Jeffrey A. Nanzer (Senior Member, IEEE) received the dual B.S. degree in electrical engineering and computer engineering from Michigan State University, East Lansing, MI, USA, in 2003, and the M.S. and Ph.D. degrees in electrical engineering from The University of Texas at Austin, Austin, TX, USA, in 2005 and 2008, respectively.

From 2008 to 2009, he was a Post-Doctoral Fellow with the Applied Research Laboratories, The University of Texas in Austin, designing electrically small HF antennas and communications systems.

From 2009 to 2016, he was with the Applied Physics Laboratory, Johns Hopkins University, Baltimore, MD, USA, where he created and led the Advanced Microwave and Millimeter-Wave Technology Section. In 2016, he joined the Department of Electrical and Computer Engineering, Michigan State University, where he held the Dennis P. Nyquist Assistant professorship from 2016 to 2021. He is currently an associate professor. He directs the Electromagnetics Laboratory, Michigan State University, which consists of the Antenna Laboratory, the Radar Laboratory, and the Wireless Laboratory. He has published more than 200 refereed journal articles and conference papers, two book chapters, and the book *Microwave and Millimeter-Wave Remote Sensing for Security Applications* (Artech House, 2012). His research interests are in the areas of distributed phased arrays, dynamic antenna arrays, millimeter-wave imaging, remote sensing, millimeter-wave photonics, and electromagnetics.

Dr. Nanzer was a Founding Member and the First Treasurer of the IEEE APS/MTT-S Central Texas Chapter. He is a member of the IEEE Antennas and Propagation Society Education Committee and the USNC/URSI Commission B. He was a recipient of the Google Research Scholar Award in 2022, the IEEE MTT-S Outstanding Young Engineer Award in 2019, the DARPA Director's Fellowship in 2019, the National Science Foundation (NSF) CAREER Award in 2018, the DARPA Young Faculty Award in 2017, and the JHU/APL Outstanding Professional Book Award in 2012. He has served as the Vice-Chair of the IEEE Antenna Standards Committee from 2013 to 2015 and the Chair of the Microwave Systems Technical Committee (MTT-16), IEEE Microwave Theory and Techniques Society, from 2016 to 2018. He was a Guest Editor of the Special Issue on Radar and Microwave Sensor Systems in the IEEE MICROWAVE AND WIRELESS COMPONENTS LETTERS in 2022. He is an Associate Editor of the IEEE TRANSACTIONS ON ANTENNAS AND PROPAGATION. He is a Distinguished Microwave Lecturer of the IEEE Microwave Theory and Techniques Society (Tatsuo Itoh Class of 2022–2024).